Applied Catalysis B: Environmental 178 (2015) 100–107

Contents lists available at ScienceDirect

Applied Catalysis B: Environmental

journal homepage: www.elsevier.com/locate/apcatb

Zeolite–TiO_2 hybrid composites for pollutant degradation in gas phase

I. Jansson[a], S. Suárez[a,*], F. Javier Garcia-Garcia[b], B. Sánchez[a]

[a] CIEMAT-Renewable Energy Division, FOTOAIR-CIEMAT, Group of Photocatalytic Treatment of Pollutant in Air, Avda. Complutense, 40, 28040 Madrid, Spain
[b] ICTS-CNME, Universidad Complutense de Madrid, 28040 Madrid, Spain

ARTICLE INFO

Article history:
Received 22 July 2014
Received in revised form 7 October 2014
Accepted 8 October 2014
Available online 24 October 2014

Keywords:
Photocatalysis
Zeolites
TiO_2
VOC

ABSTRACT

This work presents a thorough assessment of the photocatalytic properties of a series of zeolite/TiO_2 composites for the degradation of pollutants in gas phase. The composites have been prepared by the incipient wet impregnation method using an acidic TiO_2 sol precursor and five different zeolites. The influence of the content of TiO_2, the zeolite structure (Zeolite Y and ZSM-5) and the Si/Al ratio in the textural properties, adsorption capacity and the photodegradation activity of the zeolite/TiO_2 composites has been studied. Formaldehyde (HCHO) and a chlorinated hydrocarbon, trichloroethylene (C_2HCl_3), have been used as model volatile organic compounds (VOCs). The composites obtained have been characterised by N_2 adsorption–desorption, XRD, TGA-DTA, SEM and TEM microscopy. Electrophoretic migration measurements and adsorption ability in dynamic conditions for both model molecules was determined. The incipient wet impregnation method using a TiO_2 acidic sol is a suitable procedure to preparing well-dispersed TiO_2 nanoparticles around 5 nm onto microporous zeolites. The results shown in this work reveal that the nature of the pollutant and the physicochemical characteristic of the zeolites have a strong influence on the adsorption ability and in the photocatalytic performance of the composites, reducing the formation of non-desirable reaction by-products. An adequate balance between the surface area and adsorption ability is required in order to optimise the photocatalytic efficiency.

1. Introduction

Adsorption-photocatalyst hybrids (AHP's) are bifunctional materials based on an adsorbent and a photocatalyst with great potential for decontamination processes. When TiO_2 and an adsorbent coexist within the same material, the individual properties of these two kinds of compounds are combined. As a result a synergetic effect arises leading to an increase of the reaction rate [1]. The transfer of species from the adsorbent sites to the semiconductor or *vice versa* by the interface created between both phases is enhanced. The adequate choice of the support improves the dispersion of the photoactive phase, increasing the surface area and pore volume of the final material. Moreover, it may also induce modifications in the UV absorption spectrum of the semiconductor, in the acid–base characteristics, inhibiting the crystal growth. Generally adsorbents present a hydroxyl rich surface, which favour the photocatalytic process [2].

Previous studies in our group have demonstrated that sepiolite/TiO_2 (Sep/TiO_2) composites, based on a magnesium silicate and titania, exhibit better photocatalytic performance, including photoactivity, photocatalyst durability and mineralisation than benchmark TiO_2 [3–5]. With these results in mind, it is reasonable to assume that the use of adsorbents with higher surface areas could improve the behaviour of Sep/TiO_2 composites for the abatement of gas phase VOCs. In this sense, zeolites are an interesting kind of crystalline aluminosilicate minerals with high surface area and high adsorption ability so they are commonly used as adsorbents [6]. Additionally, the well-defined microporous system of the zeolites endows them with excellent shape selective properties [7].

In their seminal works, Yoneyama et al. [8,9] studied the role of porous solids with different adsorption capacities such as zeolites, activated carbon, silica and alumina for the photocatalytic degradation of propionaldehyde. They concluded that zeolite structures exhibit relevant physicochemical properties over other adsorbents such as activated carbon. Zeolites Y and ZSM-5 are some of the most commonly ordered structures used for photocatalytic studies, including the removal of nitrogen oxides [10,11], isomerisation or cyclization reactions [12,13], disinfection [14], CO_2 photoreduction [15] or the photocatalytic degradation of organic molecules [16]. Anpo et al. [17] studied hydrophilic and hydrophobic zeolite Y for the elimination of toluene and benzene

* Corresponding author. Tel.: +34 91 3466177; fax: +34 91 3466037.
E-mail address: silvia.suarez@ciemat.es (S. Suárez).

http://dx.doi.org/10.1016/j.apcatb.2014.10.022
0926-3373/

in gas phase. Xu and Langford [16,18] studied the behaviour of ZSM-5 and zeolite Y for the photodegradation of 4-chlorophenol and acetophenone in water phase. To our knowledge, the optimisation of the zeolite/TiO_2 composition and its influence on the physicochemical/adsorption properties and on the photocatalytic performance for the abatement of a typical indoor air pollutant such as formaldehyde (HCHO) and of an organochloride compound such as trichloroethylene (C_2HCl_3) in gas phase have not been reported hitherto.

Bearing in mind these observations, the objective of this work is to study the performance of different zeolite/TiO_2 composites for the photocatalytic treatment of formaldehyde and trichloroethylene in air. The optimisation of the TiO_2 loading, the effect of the zeolite structure and the Si/Al ratio were related to the textural properties and adsorption ability of the composites.

2. Experimental

2.1. Photocatalysts preparation

Two commercially available zeolites, zeolite Y (a FAU type zeolite with SiO_2/Al_2O_3 = 5–80, producer's codes: CBV 600 and CBV 780) and ZSM-5 (a MFI type zeolite with SiO_2/Al_2O_3 = 23–280, producer's codes: CBV 2314, CBV 8014 and CBV 28014) were purchased from Zeolyst. The TiO_2 sol used for the synthesis of the hybrid materials was synthetized as described elsewhere [19]. Briefly, the TiO_2 sol was synthesised by adding titanium isopropoxide to an aqueous solution of HNO_3 to a volume ratio of 900:6.5:74 (H_2O:HNO_3:TIP) [20]. Then, the suspensions were stirred for about 24 h until complete peptisation. The acidic sols were dialysed to a final pH of 3.0. The addition of a TiO_2-sol volume to the adsorbent was performed by incipient wet impregnation procedure using the pore volume values calculated by N_2 adsorption–desorption measurements for each zeolite. Thus, the desired volume of the TiO_2 sol was slowly added and mixed with the raw material. In order to eliminate the solvent and inorganic precursors used for the preparation of the composites, the solid obtained were thermally treated at 500 °C in air during 3 h. This thermal protocol was set after the TGA-DSC analyses. The TiO_2 amount in the final samples ranged between 2 and 16 wt.%. The samples with the higher amounts of TiO_2 were prepared by successive incipient impregnation processes, and the composites obtained after each impregnation step were thermally treated under air at 100 °C for 60 min previous to the next impregnation. Additionally, the TiO_2-sol was evaporated and dried at r. t. obtaining a TiO_2 xerogel that was calcined at 350 °C during 3 h. The solid recovered is referred to as TiO_2–Xg. Table 1 shows the nomenclature and selected physicochemical properties of the samples under study. Samples Z1 and Z2 identify different commercial zeolites Y with different Si/Al ratios. Z3, Z4 and Z5 identify ZSM-5 type zeolites with different Si/Al ratios. The hybrid zeolite/TiO_2 composites are identified by the prefix I- (from impregnation) followed by a number indicative of the amount TiO_2 in the composite. A commercial TiO_2 (Millenium) and a Sep/TiO_2 50:50 wt.% composite calcined at 500 °C have been used for comparison [3].

2.2. Physicochemical characterisation

The raw materials and the composited obtained have been characterised by N_2 adsorption–desorption isotherms, XRD, TGA-DTA, SEM-EDX, TEM and electrophoretic migration. The specific surface area, the average pore radius and pore volume of selected materials have been determined by N_2 adsorption–desorption at −196 °C in a Micromeritics Asap 2420 Analyser outgassing the samples overnight between 120 and 250 °C to a pressure of $<1.33 \times 10^{-2}$ Pa to ensure a clean dry surface, free from any loosely bound adsorbed species. Crystal structure identification studies were conducted with a PANalytical X'Pert PRO ultrafast detector X-ray difractometer (XRD) with CuKα radiation operating at 45 kV and 40 mA. Bragg's angles (θ) between 20° and 80° were recorded at a rate of 0.02° per step and a count time of 50 s per step. Diffraction lines were assigned to the corresponding crystalline phases by comparison with Powder Diffraction Files (PDF) from the International Centre for Diffraction Data (ICDD) Joint Committee on Power Diffraction Standards (JCPDS)).

Thermogravimetric analysis were carried out with a Mettler Toledo TGA/SDTA851e thermobalance under a controlled atmosphere within a temperature programme between 25 and 1000 °C, with a heating rate of 10 °C min^{-1} and air flow 75 mL min^{-1}.

The scanning electron microscopy characterisation was carried out in a JEOL JSM-7600F. The electron microscope is equipped with an INCA detector for energy dispersive X-ray spectroscopy, EDX. Specimens were prepared by depositing a small amount of the powder onto a clean surface graphite sample holder. Transmission electron microscopy studies were carried out in a JEOL JEM-3000F operated at 300 kV. Powder samples were ultrasonically dispersed in butanol and one drop of the resulting suspension was deposited onto a copper grid coated with a thin holey amorphous carbon layer. Images were recorded with a slow scan CCD camera. The chemical composition of the samples was determined by X-ray fluorescence using a PANalitycal axios (XFR) spectrometer, equipped with a Rh anode and 4 kW power. Zeta potential measurements were performed with a Zetasizer Nano ZS90 with a MPT-2 autotitrator. Experiments were carried out using 30 mg of 1 μm powder samples suspended in 200 mL of 10^{-3} M KCl solution, adjusting the pH value with 0.2 M and 0.02 M KOH and HCl solutions. Each curve was recorded at least three times to ensure reproducibility.

2.3. Photocatalytic activity tests

The photocatalytic performance was evaluated in a continuous flat stainless steel reactor with 120 mm × 50 mm × 10 mm (length × wide × depth) external dimensions covered by a 37 cm^2 borosilicate glass window [3]. A borosilicate glass surface of 19 cm^2 was covered by only 30 mg of composite in order to minimise the adsorption step. The samples were irradiated by two UV lights (8 W Philips) resulting in an irradiance of 6.5 mW cm^{-2}. Gas cylinders (Air Liquide) with controlled compositions HCHO/N_2 (40 ppm) or C_2HCl_3 (250 ppm) were used for pollutant feeding. 15 ppm of formaldehyde (FMD) and 25 ppm of trichloroethylene with total gas flow ranging between 100 and 900 mL min^{-1} (t_r = 0.3–3.9 s) were fed in the photocatalytic reactor.

In order to estimate the adsorption ability of the raw materials and the zeolitic composites for the model VOC molecules, adsorption experiments under realistic dynamic conditions were carried out. The experimental device was the same as that used for the photocatalytic tests. A total gas flow of 700 mL min^{-1} containing HCHO and C_2HCl_3 concentration of 15 ppm or 25 ppm respectively was used. In an initial step, the material was pre-treated during 12 h under air atmosphere and UV-A irradiation in order to remove water and weakly adsorbed organic molecules at the material surface. Then, the VOC/air gas mixture was introduced in the experimental set-up by-passing the reactor. Once a stable inlet concentration value was attained, the gas mixture was passed through the reactor containing the sample. The adsorption process commences leading to a decrease of the VOC concentration followed by a progressive increase until saturation of the material. The integration of the area above the curve allowed to calculate the amount of VOC adsorbed (Table 1). Once the steady-state conditions were achieved, the UV lamps were switched on commencing thus the photocatalytic reaction. The evolution of the concentration of the

Table 1
Properties of the reference materials and the zeolite/TiO_2 composites heat treated at 500 °C

Sample	Adsorbent	SiO_2/Al_2O_3[a]	TiO_2 (wt.%)	BET area ($m^2\ g^{-1}$)	V_p ($cm^3\ g^{-1}$)			Pore mean size (nm)		Adsorption ($\mu mol\ g^{-1}_{catal}$)	
					V_T	Micro[b]	Meso	Micro[b]	Meso	HCHO	C_2HCl_3
Raw materials											
Z1	Zeolite Y	5	–	669	0.39	0.25	0.14	0.74	10	832	115
Z2	Zeolite Y	80	–	872	0.56	0.36	0.20	0.75	17	74	62
Z3	ZSM-5	23	–	404	0.19	0.14	0.05	0.51	–	620	400
Z4	ZSM-5	80	–	456	0.26	0.18	0.08	0.55	–	136	358
Z5	ZSM-5	280	–	402	0.17	0.14	0.03	0.60	–	51	300
TiO_2	–	–	100	152	0.39	–	0.26	–	7.0/13.0	1940	78
TiO_2–Xg	–	–	100	149	0.24	–	0.28	–	7.0/–	535	5
Sep/TiO_2	Sepiolite	–	50	153	0.62	–	0.40	–	15/45	212	18
Zeolite/TiO_2 composites											
Z1I3	Zeolite Y	5	8	589	0.41	0.22	0.19	0.66	12	557	80
Z2I3	Zeolite Y	80	8	776	0.51	0.30	0.21	0.69	14	259	29
Z3I1	ZSM-5	23	2	n.a.	n.a.	n.a.	n.a.	n.a.	n.a.	n.a.	n.a.
Z3I2	ZSM-5	23	4	390	n.a.	n.a.	0.08	n.a.	n.a.	581	n.a.
Z3I3	ZSM-5	23	8	379	0.24	0.15	0.09	0.47	–	673	331
Z3I4	ZSM-5	23	16	274	n.a.	n.a.	0.15	n.a.	–	700	n.a.
Z4I3	ZSM-5	80	8	422	0.27	0.16	0.11	0.49	–	327	300
Z5I3	ZSM-5	280	8	338	0.24	0.15	0.09	0.48	–	322	271

[a] SiO_2/Al_2O_3 mole ratio.
[b] Calculated by the Horvath–Kawazoe (HK) method.
n.a.: not analysed.

pollutants and the formation of reaction products at different gas flows was continuously monitored. The gas-phase composition was measured by using a FTIR Thermo-Nicolet 5700 spectrometer, provided with a temperature controlled multiple-reflection gas cell (optical path 2 m) maintained at 110 °C. IR spectra were registered after accumulation of 64 scans at a resolution of 4 cm^{-1}. The evolution of the reaction products during the reaction was monitored by following the evolution of the representative vibrational bands of selected molecules. HCHO photodegradation was monitored by following the bands at 1842–1623 cm^{-1} along with the characteristic vibration of the CO_2 band at 2435–2233 cm^{-1}. The photodegradation of C_2HCl_3 was monitored by following the bands at 965–903 cm^{-1}, the bands for CO_2 at 2435–2233 cm^{-1} and the bands for $COCl_2$ at 1873–1780 cm^{-1}.

Formaldehyde and trichloroethylene conversion values were calculated according the following equation:

$$\text{Conversion VOC}\,(\%) = \frac{C_{inlet} - C_{outlet}}{C_{inlet}} \times 100 \quad (1)$$

where C_{inlet} and C_{outlet} were the concentration of VOC in the reactor inlet and outlet, respectively. In the case of trichloroethylene photodegradation, the selectivity to $COCl_2$ was calculated as described previously [4,5]:

$$\text{Selectivity}\,COCl_2\,(\%) = \frac{C_{COCl2}}{2 \times (C_{inlet} - C_{outlet})} \times 100 \quad (2)$$

3. Result and discussion

The most relevant textural and physicochemical properties of the raw materials and of the zeolite/TiO_2 composites treated at 500 °C under air are shown in Table 1. The TGA-DSC analyses for Z1–Z5 (not shown) indicate that commercial zeolites are stable within this temperature range.

In order to evaluate the influence of zeolite's structure and of the Si/Al ratio on the photocatalytic performance of the hybrid materials, zeolites with the FAU and MFI structures (zeolite Y and zeolite HZSM-5, respectively) were selected. The BET areas of the commercial zeolites (Z1 to Z5) range between 400 and 880 $m^2\ g^{-1}$. This feature could be indicative of the presence of some amorphous silica and alumina phases in the commercials zeolites. As shown in Table 1, all of the zeolites Y (Z1-Z2) exhibit higher surface areas and greater pore volume values than ZSM-5 zeolites (Z3–Z5). Zeolite Y and ZSM-5 are microporous materials having pores of, 0.7 nm and 0.5 nm, respectively, in good agreement with previously reported values [21].

The commercial Y zeolites used in this work (Z1-Z2) and, as a consequence, the zeolite Y-based materials also contain mesopores of 10–17 nm. The presence of such mesopores is probably due to a dealumination processes during the synthesis process, probably carried out in order to obtaining the desired Si/Al ratio. On the other hand, the specific surface areas of the commercial TiO_2, the TiO_2 xerogel obtained from the dehydration of the TiO_2 sol and of the Sep/TiO_2 composite, are significantly smaller, typically in the range of 150 $m^2\ g^{-1}$. All of these solids have a large contribution of mesopores due to the separation of particles or aggregates [22,23].

Regarding the formaldehyde adsorption it is important to remark the high HCHO adsorption values for commercial TiO_2 following by Z1 (zeolite Y $SiO_2/Al_2O_3 = 5$) and Z3 (ZSM-5 $SiO_2/Al_2O_3 = 23$). It is well-known that electrostatically polarised or unbalanced sites of zeolites behave as strong adsorption sites for polar molecules such as formaldehyde [14]. On the contrary, the TiO_2 adsorption ability for trichloroethylene adsorption is significantly lower than for HCHO, highlighting the properties of MFI type structures over FAU. The adsorption ability for both VOC is independent of the surface area. Moreover, an inverse relationship between the FMD and TCE adsorption capacity with the Si/Al ratio and total pore volume was observed. Takeuchi et al. have suggested that toluene or benzene adsorption is closely dependent on the surface area rather than other surface properties [17]. However, our results are not in line with this observation probably due to as the Si/Al ratio increases, unit cell size shrinks, and the void volume for VOC adsorption decrease. Zeolite/TiO_2 composites show the general trend observed for raw materials with a subsequent reduction of the BET area by incorporation of the semiconductor. The large surface area of the ordered micropore structure was maintained due to the low amount of TiO_2 incorporated on the zeolite matrix.

3.1. Influence of the TiO_2 loading

The influence of TiO_2 loading on the textural, adsorption and photocatalytic properties of the zeolite/TiO_2 hybrid composites has been analysed. Fig. 1a and b show representative N_2

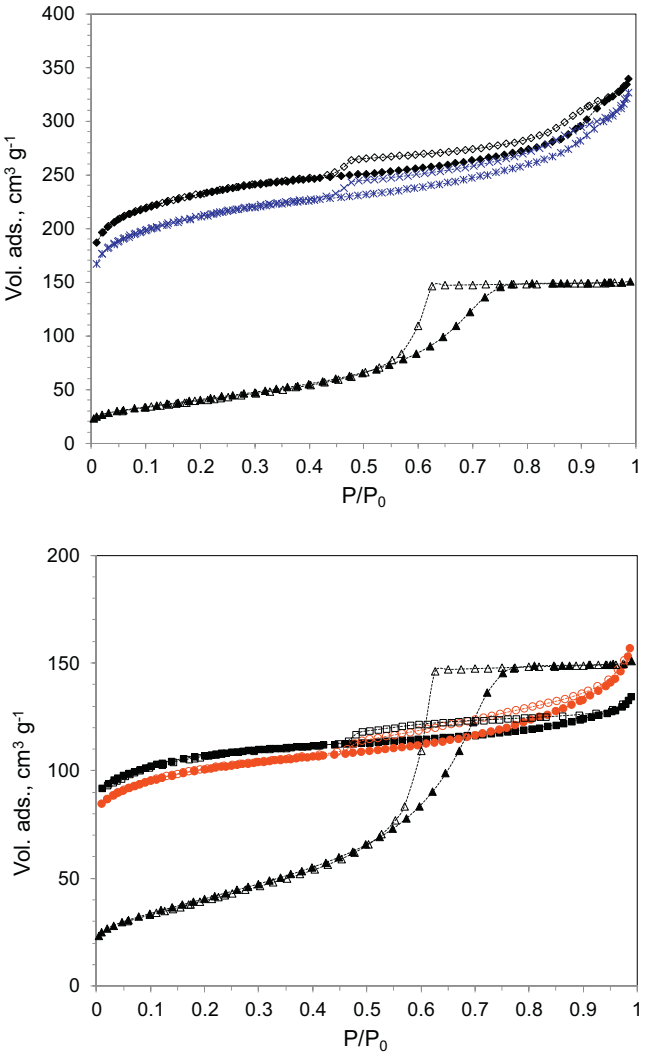

Fig. 1. N_2-adsorption–desorption isotherms for zeolite/TiO_2 composites: (a) Zeolite Y (♦,◊) Z2, (*,x) Z2I3 and (b) ZSM-5 (■,□) Z3, (●,○) Z3I3. Reference: (▲,△) TiO_2–Xg.

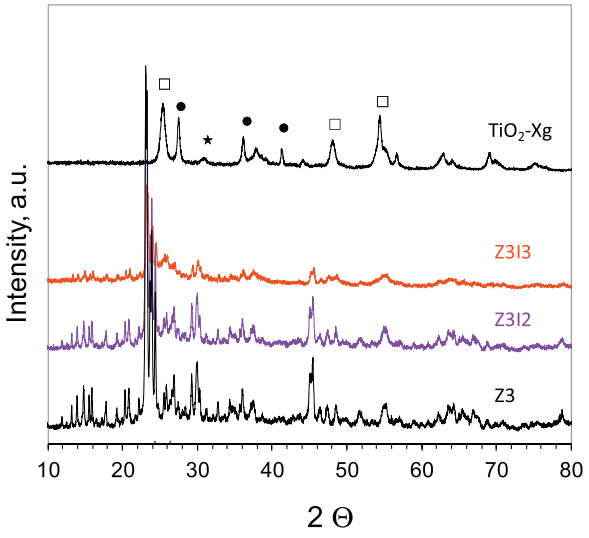

Fig. 2. X-ray difractograms of zeolite/TiO_2 composites. TiO_2–Xg is included for comparison: (□) TiO_2-anatasa, (•) TiO_2-rutile and (*) TiO_2-brookite.

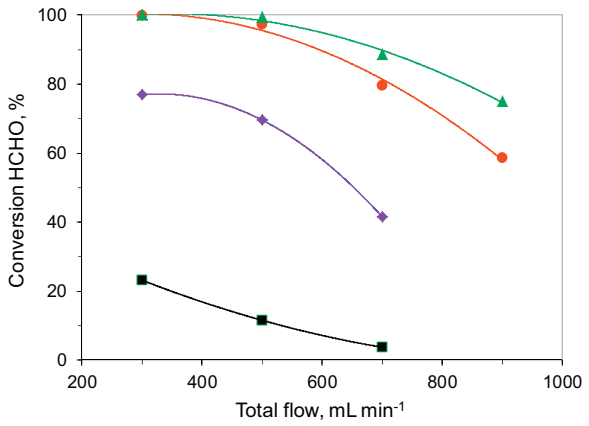

Fig. 3. Effect of TiO_2 loading on the photodegradation of formaldehyde for Z3/TiO_2 composites (■) Sep/TiO_2, (♦) Z3I2, (●) Z3I3, (▲) Z3I4.

adsorption–desorption isotherms recorded for zeolite Y (Z2, Z2I3) and Z3 and Z3I3 samples respectively. TiO_2–Xg was included for comparison. In order to avoid overlapping of the curves, the isotherm corresponding to others TiO_2 amount were not included. According to the IUPAC classification, all zeolites present a Type I isotherm characteristic of microporous solids [24] with a H4 hysteresis cycle closed at 0.4 partial pressure which is, in the case of type I isotherms, a sign of microporosity. Clearly, the zeolite Y-based composite Z2I3 has a higher degree of microporosity than Z3I3, which is based upon ZSM-5. The TiO_2–Xg records a type IV isotherm, characteristic of mesoporous materials, with a H2 type hysteresis loop, indicative of the presence of spherical particles with the so-called "ink bottle" pores type and a pores size of 7.0 nm [22]. Finally, zeolite/TiO_2 composites record a slight reduction of the total pore volume as compared to that of the parent zeolites, probably due to the pore blocking by the TiO_2 particles.

Fig. 2 shows the X-ray diffraction patterns for Z3 and Z3 based TiO_2 composites (Z3, Z3I2/TiO_2 and Z3I3/TiO_2). The difractograms of the TiO_2–xerogel is also shown. MFI or FAU (not shown) type structures were identified in the difractograms of all samples [25,26]. The TiO_2 xerogel shows the characteristic diffraction lines of TiO_2-anatase (1 0 1) (0 0 4) (2 0 0) planes, with a minor contribution of the brookite phase (1 2 1), and of the rutile phase (1 1 0) (1 0 1) [22]. The difractograms of the Z3/TiO_2 composites also show the characteristic diffraction lines of ZSM-5. A slight decrease in the intensity of the diffraction lines characteristic of the ZSM-5 type structure after the incorporation of an 8 wt.% TiO_2 was observed. This dilution effect is more evident for the TiO_2 crystal phases. In fact the characteristic diffraction lines of TiO_2 are not observed in the difractograms of the Z3-based/TiO_2 composites. Although not shown, similar difractograms have been obtained for the composites prepared with the other ZSM-5 (Z4 and Z5 series) and with zeolite Y (Z1 and Z2 series). The lack of characteristic X-ray peaks for TiO_2 suggests that TiO_2 is well dispersed over the zeolite, which in fact prevents the growing of large TiO_2 crystallites as previously observed for Sep/TiO_2 composites [23].

In order to optimise the TiO_2 loading, the photocatalytic properties of the hybrid composites for the degradation of formaldehyde in gas phase at different air flows were evaluated. Experiments were conducted at different residence times between 3.9 and 0.3 s keeping constant the amount of photocatalyst in the reactor. Fig. 3 shows the evolution of the HCHO conversion with total flow recorded for the Z3-based/TiO_2 hybrid composites (Z3I2, Z3I3 and Z3I4) and with Sep/TiO_2. Under the studied conditions all composites show measurable HCHO conversion which decrease with the increasing total gas flow.

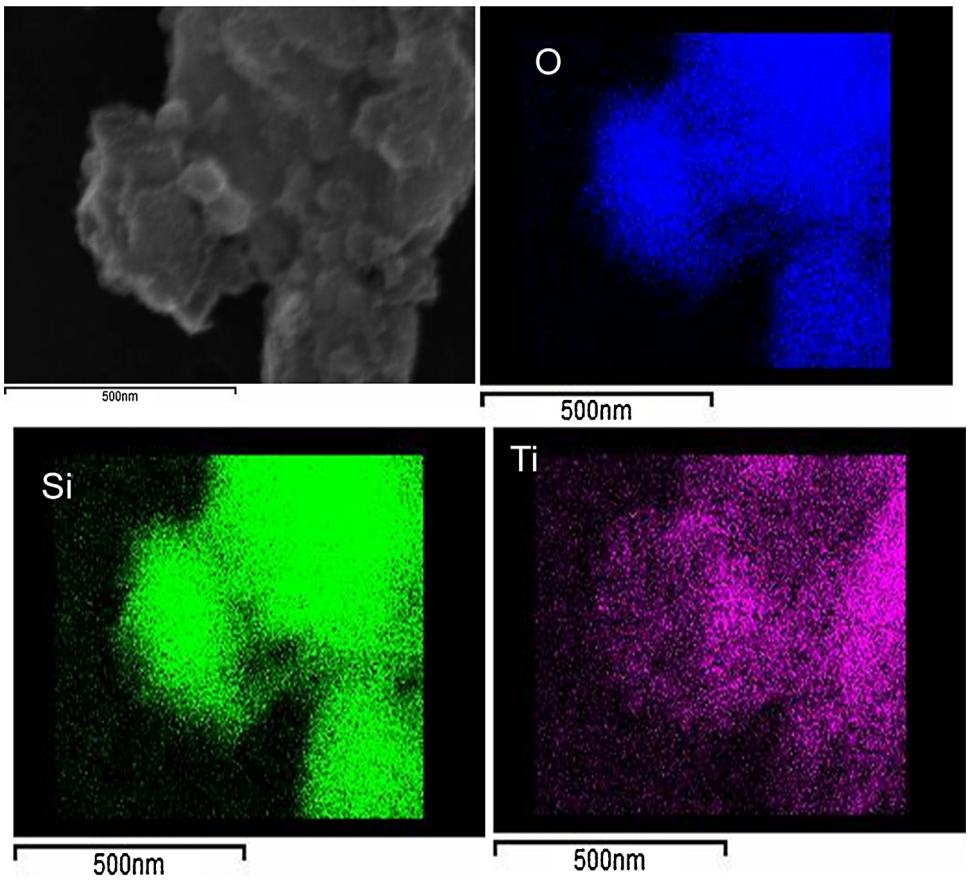

Fig. 4. SEM-EDX micrographs obtained for Z3I3 composite.

According to literature, the main oxidative (Eqs. (4) and (5)) and reductive processes (Eq. (6)) involved in the photocatalytic degradation of formaldehyde are [27–29]:

$$TiO_2 \xrightarrow{h\nu} e^- + h^+ \quad (3)$$

$$HCHO + H_2O + 2h^+ \rightarrow HCOOH + 2H^+ \quad (4)$$

$$HCOOH + 2h^+ \rightarrow CO_2 + 2H^+ \quad (5)$$

$$\frac{1}{2}O_2 + 2e^- + 2H^+ \rightarrow H_2O \quad (6)$$

In all cases total mineralisation was attained and reaction products other than CO_2 were not detected under the operating conditions selected. Noguchi et al. detected formic acid at the TiO_2 surface as a partial oxidation by-product [29]. However, under the adequate operating conditions (residence time, UV irradiation) all of the intermediates and by-products can be oxidised to CO_2. It should be remarked that none of the raw zeolite materials (Z1–Z5) record measurable HCHO conversions under these reaction conditions. The reference Sep/TiO_2 shows a significantly lower photocatalytic activity than that recorded for the zeolite/TiO_2 composites. As shown in Fig. 3, the photocatalytic performance increases with the increasing amount of TiO_2 in the composite. The addition of a low amount of TiO_2 of 4 wt.% to Z3 results in a significant photodegradation of HCHO with a maximum conversion value of around 80%. A further increasing of TiO_2 loading to 8 wt.% increases HCHO conversion significantly around a 40% (sample Z3I3). However, increasing TiO_2 content to 16 wt.% only results in a moderate increasing of HCHO conversion, probably due a limitation in the number of adsorbed photons by TiO_2 [30]. According to these results, the optimum titania loading was set to 8 wt.% for further studies.

The TiO_2 incorporation on the zeolites was analysed by electron microscopy. Fig. 4 depicts a SEM-EDX compositional mapping of O, Si and Ti in a typical aggregate of Z3I3 particles. Clearly, titanium is homogeneously distributed all over the zeolite matrix. The morphology of the zeolite/TiO_2 composites (both for zeolite Y and ZSM-5) has been analysed by TEM. The images obtained with Z2I3 and Z3I3, which are representative for all zeolite Y and ZSM-5 composites, are depicted in Fig. 5a and b, respectively. In addition, the microstructure of the raw zeolite Y is shown in Fig. 5a (back figure). The ordered micropore structure of the zeolitic materials with channels of 0.55 nm or 0.75 nm for zeolites ZSM-5 and Y, respectively, can be observed. Irrespective of the nature of the zeolite, homogeneously distributed TiO_2 nanoparticles with mean particle sizes of around 5 nm can be clearly distinguished in all composites. This observation is in good agreement with the results derived from the SEM-EDX analysis which show a homogeneous distribution of the TiO_2 particles on the zeolites. The nanometric size of the TiO_2 domains explains why the lack of diffraction peaks for TiO_2 phases in the X-ray difractograms of the hybrid composites. These results reveal that the incipient wet impregnation method using a TiO_2 acidic sol is a suitable method to preparing well-dispersed TiO_2 nanoparticles onto microporous zeolites.

3.2. *Influence of the zeolite type structure and Si/Al ratio on the photoactivity*

In order to determine the influence of the zeolite nature (zeolite Y *vs.* ZSM-5 with the same Si/Al ratio) and the effect of the Si/Al ratio on the photocatalytic activity of the hybrid composites, the zeolite/TiO_2 composites with 8 wt.% TiO_2 loading were evaluated (see Table 1). The photocatalytic performances were

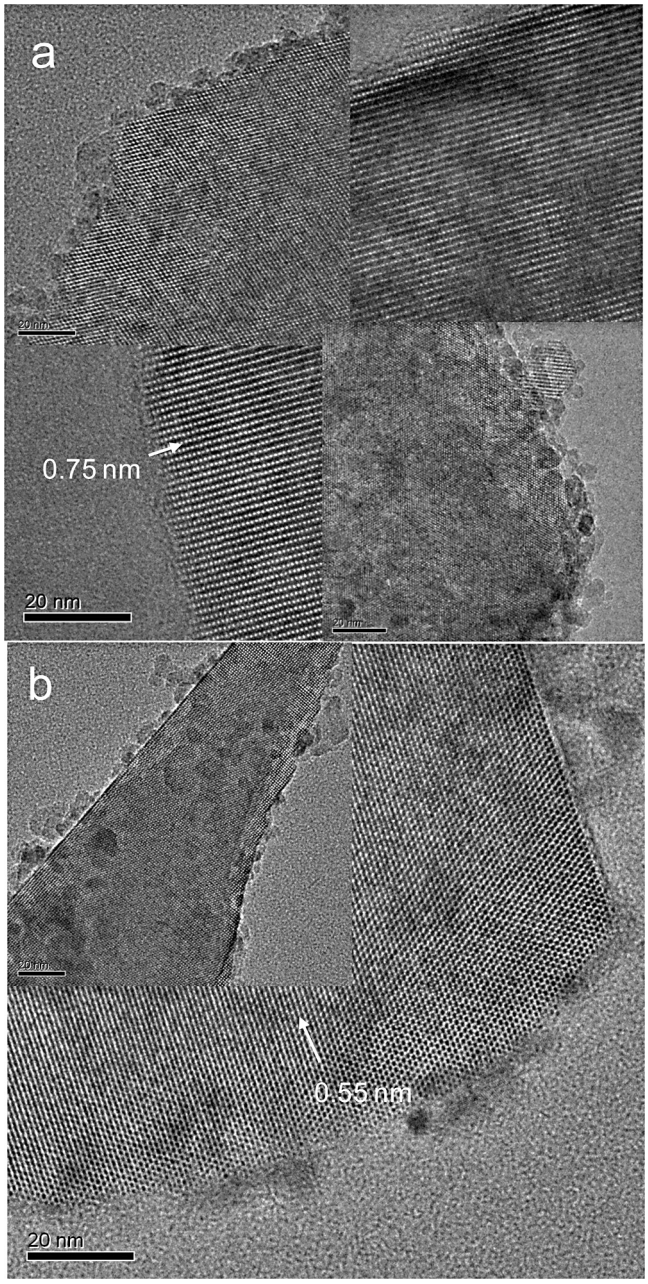

Fig. 5. TEM micrographs for (a) Z2 (back), Z2I3 (front) and (b) Z3I2 zeolite/TiO_2 composites.

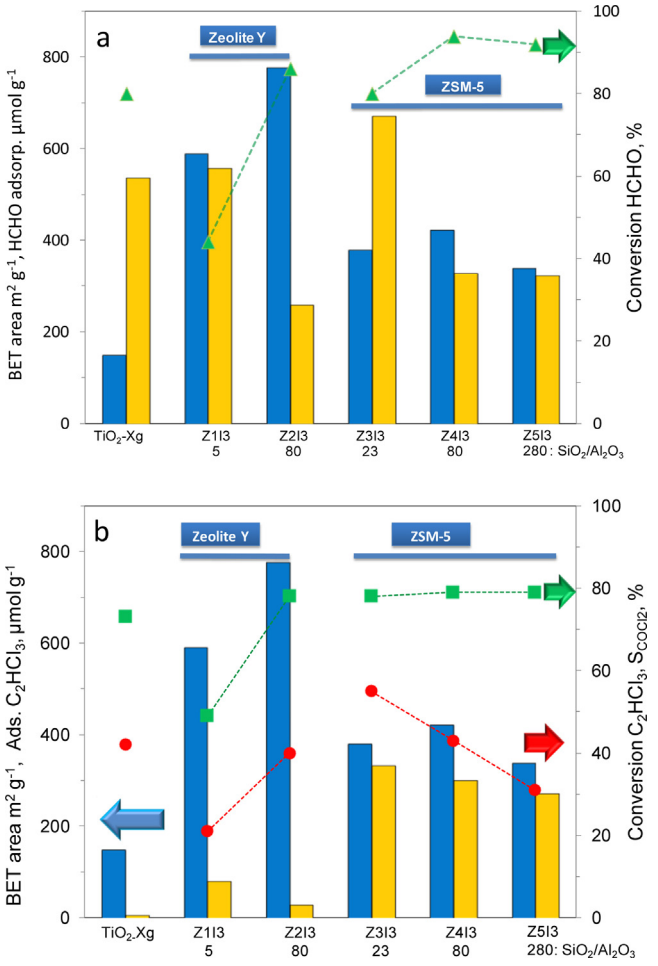

Fig. 6. Relationship between the zeolite nature and Si/Al ratio on the surface area, adsorption ability and photocatalytic activity for: (a) formaldehyde degradation at 700 mL min^{-1} and (b) trichloroethylene elimination at 500 mL min^{-1}. ( ) BET area, ( ) HCHO or C_2HCl_2 adsorption of (▲) HCHO conversion, ( ) C_2HCl_3 conversion and (●) $COCl_2$ selectivity.

measured under the same conditions than those for the photocatalysts depicted in Fig. 3, *i.e.*, total flow between 300–900 mL min^{-1}. VOC (formaldehyde or trichloroethylene) conversions obtained at 700 and 500 mL min^{-1}, respectively, are shown in Fig. 6. Fig. 6 also shows the specific surface areas of the catalyst and their adsorption ability towards either formaldehyde or trichloroethylene. The performance of TiO_2–Xg is shown for comparison. TiO_2–Xg has a good photoactivity for the degradation of formaldehyde with conversion value of around 80%. Remarkably, and despite of the significantly lower amount TiO_2 on the zeolite/TiO_2 composites (8 wt.%) all zeolite/TiO_2 composites record higher photoactivity than TiO_2–Xg for the degradation of formaldehyde. Only Z1I3 shows a poor HCHO conversion compared to TiO_2–Xg. In fact, if data conversion data (µmol HCOOH converted) are normalised to the total amount of TiO_2 in the samples, Z3I3 shows a value of 2.7 µmol $g^{-2}{}_{TiO2}$ s^{-1} whereas TiO_2–Xg records only 0.2 µmol $g^{-2}{}_{TiO2}$ s^{-1} for TiO_2–Xg.

The study of the influence of the SiO_2/Al_2O_3 ratio in the catalytic performance of the hybrid composites was conducted with samples Z2I3 and Z4I3 (SiO_2/Al_2O_3 = 80). As observed in Fig. 6a, Z4I3 exhibits better photocatalytic performance for the photodegradation of HCHO than Z2I3. Similar results have been reported by Kuwahara and Yamashita [31]. Fig. 6a also illustrates how the Si/Al ratio is very important for the photoactivity of the composites. Thus, an increase of the HCHO conversion of around 10% was achieved when the SiO_2/Al_2O_3 ratio increases from 23 to 80 in the ZSM-5/TiO_2 composites. However, HCHO conversion remains roughly constant for the composites with higher SiO_2/Al_2O_3 ratio. Similar trends than those reported in Fig. 6a have been observed for the reactions conducted at 900 mL min^{-1}.

It is worth to remark that the adsorption capacity of the composites decreases with the increasing Si/Al ratio leading, however, to more photoactive materials. The results obtained for the photooxidation of HCHO indicate that a strong adsorption of HCHO onto the zeolite component of the composite prevents its access to the photocatalytic active sites of the TiO_2 phase therefore decreasing the reaction rate. Our results, suggests that an adequate balance between the surface area and adsorption ability is required in order to obtain an optimum photoefficiency.

Surprisingly, zeolite Y with SiO_2/Al_2O_3 = 5 which shows the highest adsorption capacity and a surface area near 600 m^2 g^{-1}, records a rather poor photoactivity for the oxidation of HCHO. In

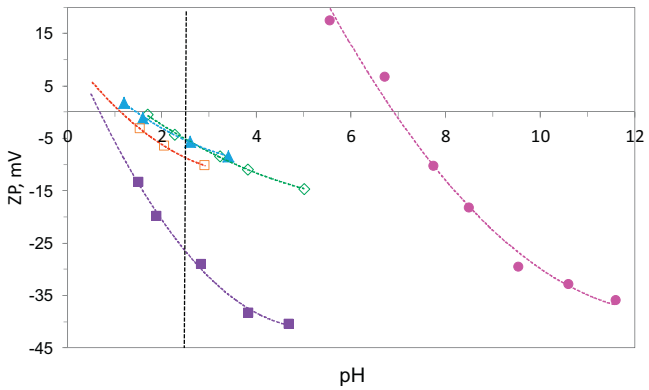

Fig. 7. Variation of zeta potential with pH for commercial zeolite: (●) Z1, (◇) Z2, (▲) Z3, (□) Z4, (■) Z5.

order to understand this behaviour, electrophoretic migration measurements were conducted with Z1–Z5 zeolites. In Fig. 7, the results of the variation of the zeta potential with the pH for commercial zeolites are shown. A decrease of the isoelectric point with the aluminium content was observed in the zeta potential curves [32]. As observed, all zeolites present an isoelectric point below the pH at which the TiO_2 sol was synthetized (pH = 3.0). Only zeolite Z1 exhibits an isoelectric point at pH = 7. The measurement of the surface net charge for the TiO_2 sol at pH = 3 results in a zeta potential value of +50 mV. Thus, TiO_2 nanoparticles with a net positive charge are predominant in the TiO_2 sol. The interaction with the negatively charged (at pH = 3) zeolites (Z2–Z5) is therefore promoted. By contrary, Z1 and TiO_2 nanoparticles are positively charged at pH = 3 thus preventing the interaction between TiO_2 and zeolite Z1.

The behaviour of the composites in the photodegradation of trichloroethylene was also investigated. Trichloroethylene photooxidation is, however, more complicated reaction than HCHO photooxidation since, besides CO_2, others non-desirable by-products are formed [33]. The ideal reaction is shown in Eq. (7) where TCE is mineralised into CO_2 and HCl with participation of adsorbed water or superficial hydroxyl groups [34]. However, others chlorinated partial oxidation reaction products have been identified such as $COCl_2$ (carbonyl dichloride or phosgene), C_2HCl_3O (dichloroacetyl chloride or DCAC) besides CO, HCl [33]. It is assumed that $OH^\bullet$ and $Cl^\bullet$ radicals initiate the reaction going through the formation of DCAC (Eq. (8)) that can be further oxidised to produce $COCl_2$ (Eq. (9)).

$$C_2HCl_3 + \frac{3}{2}O_2 + H_2O \xrightarrow{h\nu,TiO_2} 2CO_2 + 3HCl \quad (7)$$

$$C_2HCl_3 + \frac{1}{2}O_2 \xrightarrow{h\nu,TiO_2} Cl_2HCCOCl \quad (8)$$

$$Cl_2HCCOCl + \frac{1}{2}O_2 \xrightarrow{h\nu,TiO_2} COCl_2 + HCl + CO \quad (9)$$

It is well known that the formation of $COCl_2$ can be reduced by increasing the residence time, adding water vapour in the feed or by hydrolysis reactions to product CO_2 at dark conditions [35]. However, in order to accurately analyse the influence of the physicochemical properties of the zeolite/TiO_2 composites on the reaction, experiments were performed in the absence of water vapor. C_2HCl_3 conversion and selectivity to $COCl_2$ along with the adsorption capacity of composites towards C_2HCl_3 are shown in Fig. 6b. In line with the results obtained for HCHO, zeolite/TiO_2 composites are more active than TiO_2–Xg for the photodegradation of C_2HCl_3. The adsorption capacity of ZSM-5 is considerable higher than that of zeolite Y, despite the lower surface area of the former. These differences do not seem to affect the photocatalytic activity performance of the composites, since similar results were obtained for all of them, with the exception of Z1I3. This composite showed the lowest reaction rate as previously observed for the HCHO photooxidation. Unlike for HCHO degradation, the Si/Al ratio has not an apparent influence in the degradation of C_2HCl_3 with the ZSM-5 based composites Nevertheless, the $COCl_2$ selectivity decreases when the Si/Al ratio increases. In the case of Z5I3, the ones with a SiO_2/Al_2O_3 ratio of 280, the $COCl_2$ selectivity was around 10% lower than for bare TiO_2. These differences become more obvious, one order of magnitude higher, if the reaction rates are normalised to the actual amount of TiO_2 in the catalyst. These results point out that the Si/Al ratio has a strong influence in the elimination of reaction by-products. It has been reported that a relationship between the Si/Al ratio and the hydrophobic nature of the zeolite exits [31]. The higher the hydrophobicity of the zeolite/TiO_2 composite the lower is the formation of organochloride by-products. Commercial zeolites Z1–Z5 were tested under the same conditions described in Fig. 6. In contrast to FMD photodegradation, commercial zeolites were able to photooxidase TCE. Z1 records a C_2HCl_3 conversion of around 35%, followed by Z4 and Z5 with conversions around 30%. Z3 and Z2 show conversions less than 10%. These results pointed out the intrinsic ability of zeolites to photodegrade this organochloride compound. It is well known that natural or synthetic zeolites and clays may contain traces of iron atoms in the structure. Thus, iron content was analysed by X-ray fluorescence. All zeolites shown similar iron amounts around 0.02%. The result seems to indicate that factors other than iron content, such as iron oxidation state or location in the zeolitic matrix should be considered in order to explain the photocatalytic performance of the zeolite.

It has been reported that oxidising species or hydrogen spillover can travel on inert surfaces, such as silicon, for quite a long distance [36,37]. Hydroxyl radicals generated on the TiO_2 surface can migrated over a siliceous matrix [38]. Haick and Paz [39,40] reported that oxidising species photogenerated on titanium dioxide well-defined microdomains, are capable of inducing the mineralisation of aliphatic chains anchored to inert silicon domains. The remote photodegradation effect was due to out-diffusion of oxidising species on the surface. It is known that zeolite catalysts can stabilise reactive intermediates in several photochemical reactions. Reactive species such as $OH^\bullet$ or O_2^-, which are formed during TiO_2 photocatalysis, may be stabilised within the rigid framework of the zeolite, where the adsorbed organic molecules can then be efficiently reached by these reactive species [18]. Moreover, oxygen adsorption in the zeolite is essential to the electron accepting process on the TiO_2. In line with our previous results obtained for magnesium silicate [3], because of its adsorbent properties zeolite may acts as a buffer of VOC. Zeolite domains retain a constant VOC concentration in the vicinity of TiO_2 photoactive sites, allowing the diffusion of non-desirable reaction products when formed, and probably with the subsequent reaction with reactive species such as $OH^\bullet$ or O_2^-.

4. Conclusions

Incipient wet impregnation of commercial zeolites with an acidic TiO_2 sol is an effective and efficient method to immobilise TiO_2 nanoparticles of around 5 nm particle size, homogeneously distributed on zeolitic structures. The determination of the isoelectric point of the commercial zeolites is a fundamental parameter to understand the deposition of TiO_2 nanoparticles on the zeolitic matrix. Zeolite/TiO_2 hybrid composites exhibit excellent photocatalytic performances for the degradation of both, formaldehyde and trichloroethylene in gas phase. TiO_2 content as low as 8 wt.% in the zeolite/TiO_2 hybrid composites is enough to promote the photocatalytic activity of bare TiO_2.

The performance of zeolite/TiO_2 hybrid composites for VOCs elimination can be improved by the adequate choice of the zeolite type and the Si/Al ratio. A direct relationship between the Si/Al ratio and the photodegradation of formaldehyde with a subsequent reduction of the $COCl_2$ formation during trichloroethylene degradation is observed. This effect is mainly related to the hydrophobic nature of the zeolites. A balance between the surface area and adsorption ability is required in order to optimise the photocatalytic efficiency. These results pointed out the importance of the diffusion of the pollutant, reaction products and oxidising species between both components.

Acknowledgment

Authors are grateful to the Spanish Ministry of Economy and Competitiveness for the financial support (projects CTM 2011-25093, IPT-2011-1568-310000), Mss. Jansson for the PhD grant (BES-2012-055758) and Dra. Suárez for the Ramón & Cajal Contract. The Research Support Unit from the ICP-CSIC is acknowledged for XRD and BET analysis. Dra. I. Díaz is also acknowledged for her valuable comments.

References

[1] F. Fresno, P. Portela, S. Suárez, J.M. Coronado, J. Mater. Chem. 2 (2014) 2863–2884.
[2] S. Suárez, in: J.M. Coronado, F. Fresno, M.D. Hernández-Alonso, R. Portela (Eds.), Design of Advanced Photocatalytic Materials for Energy Conversion and Environmental Applications, Springer-Verlag, London, 2013, pp. 245–267, ISBN 978-1-4471-5060-2.
[3] S. Suárez, J.M. Coronado, R. Portela, J.C. Martín, M. Yates, P. Ávila, B. Sánchez, Environ. Sci. Technol. 42 (2008) 5892–5896.
[4] T.L.R. Hewer, S. Suárez, J.M. Coronado, R. Portela, P. Avila, B. Sanchez, Catal. Today 13 (2009) 302–308.
[5] S. Suárez, T.L.R. Hewer, R. Portela, M.D. Hernandez-Alonso, R.S. Freire, B. Sanchez, Appl. Catal. B 101 (2011) 176–182.
[6] J. Weitkamp, Solid State Ion. 131 (2000) 175–188.
[7] A. Corma, H. Garcia, Chem. Commun. 10 (2004) 1443–1459.
[8] H. Yoneyama, T. Torimoto, Catal. Today 58 (2000) 133–140.
[9] T. Torimoto, S. Ito, S. Kuwabata, H. Yoneyama, Environ. Sci. Technol. 30 (1996) 1275–1281.
[10] M. Matsuoka, E. Matsuda, K. Tsuji, H. Yamashita, M. Anpo, J. Mol. Catal. A 107 (1996) 399–403.
[11] M. Matsuoka, W.S. Ju, H. Yamashita, M. Anpo, J. Photochem. Photobiol. A 160 (2003) 43–46.
[12] K.V. Subba Rao, B. Srinivas, M. Subrahmanyam, Catal. Lett. 89 (2003) 95–102.
[13] S.G. Zhang, S. Higashimoto, H. Yamashita, M. Anpo, J. Phys. Chem. B 102 (1998) 5590–5594.
[14] G. Čík, S. Priesolová, H. Bujdáková, F. Šeršen, T. Potheöová, J. Krištín, Chemosphere 63 (2006) 1419–1426.
[15] K.D. Dubois, A. Petushkov, E. Garcia Cardona, S.C. Larsen, G. Li, J. Phys. Chem. Lett. 3 (2011) 486–492.
[16] Y. Xu, C.H. Langford, J. Phys. Chem. B 101 (1997) 3115–3121.
[17] M. Takeuchi, M. Hidaka, M. Anpo, J. Hazard. Mater. 237–238 (2012) 133–139.
[18] Y. Xu, C.H. Langford, J. Phys. Chem. 99 (1995) 11501–11507.
[19] A. Sirisuk, C.G. Hill Jr., M.A. Anderson, Catal. Today 54 (1999) 159–164.
[20] S. Yamazaki-Nishida, J.K. Nagano, L.A. Phillips, S. Cervera-March, M.A. Anderson, J. Photochem. Photobiol. A 70 (1993) 95–99.
[21] J. Čejka, A. Corma, S. Zones, Zeolites and Catalysis: Synthesis, Reactions and Applications, Wiley-VCH Verlag GmbH & Co. KGaA, Weinheim, Germany, 2010.
[22] N. Miranda-García, S. Suárez, B. Sánchez, J.M. Coronado, S. Malato, M.I. Maldonado, Appl. Catal. B 103 (2011) 294–301.
[23] S. Suárez, M. Yates, P. Avila, J. Blanco, Catal. Today 105 (2005) 499–506.
[24] G. Leofanti, M. Padovan, G. Tozzola, B. Venturelli, Catal. Today 41 (1998) 207–219.
[25] M.M.J. Treacy, J.B. Higgins (Eds.), Collection of Simulated XRD Powder Diffraction Patterns for Zeolites, 5th revised ed., Elsevier, Amsterdam, 2007.
[26] R. von Ballmoos, J.B. Higgins (Eds.), Collection of Simulated XRD Powder Diffraction Patterns for Zeolites, 2nd revised ed., Butterworth-Heinemann, Stoneham, 1990.
[27] J. Peral, D.F. Ollis, J. Catal. 136 (1992) 554–565.
[28] M.A. Aguado, M.A. Anderson, C.G. Hill Jr., J. Mol. Catal. 89 (1994) 165–178.
[29] T. Noguchi, A. Fujishima, K. Hashimoto, P. Sawunyama, Environ. Sci. Technol. 32 (23) (1998) 3831–3833.
[30] F. Haque, E. Vaisman, C.H. Langford, A. Kantzas, J. Photochem. Photobiol. A 169 (2005) 21–27.
[31] Y. Kuwahara, H. Yamashita, J. Mater. Chem. 21 (2011) 2407–2416.
[32] T. Kuzniatsova, Y. Kim, K. Shqau, P.K. Dutta, H. Verweij, Microporous Mesoporous Mater. 103 (2007) 102–107.
[33] M.D. Driessen, A.L. Goodman, T.M. Miller, G.A. Zaharias, V.H. Grassian, J. Phys. Chem. B 102 (1998) 549–556.
[34] M.R. Nimios, W.A. Jacoby, D.M. Blake, T.A. Milne, Environ. Sci. Technol. 27 (1993) 732–740.
[35] W.A. Jacoby, M.R. Nimlos, D.M. Blake, R.D. Noble, C.A. Koval, Environ. Sci. Technol. 28 (1994) 1661–1668.
[36] S. Suarez, M. Yates, A.L. Petre, J.A. Martin, P. Avila, J. Blanco, Appl. Catal. B 64 (2006) 302–311.
[37] P. Baeza, M. Villarroel, P. Ávila, A. López Agudo, B. Delmon, F.J. Gil-Llambías, Appl. Catal. A 304 (2006) 109–115.
[38] M.C. Lee, W. Choi, J. Phys. Chem. B 106 (2002) 11818–11822.
[39] H. Haick, Y. Paz, J. Phys. Chem. B 105 (2001) 3045–3051.
[40] H. Haick, Y. Paz, J. Phys. Chem. B 107 (2003) 2319–2326.